



# Chemical bonding dictates drastic critical temperature difference in two seemingly identical superconductors

Robert H. Lavroff<sup>a</sup> , Julen Munarriz<sup>b</sup> , Claire E. Dickerson<sup>a</sup>, Francisco Munoz<sup>c,d,1</sup> , and Anastassia N. Alexandrova<sup>a,e,f,1</sup>

Edited by Laura Gagliardi, The University of Chicago, Chicago, IL; received September 21, 2023; accepted January 11, 2024

Though  $\text{YB}_6$  and  $\text{LaB}_6$  share the same crystal structure, atomic valence electron configuration, and phonon modes, they exhibit drastically different phonon-mediated superconductivity.  $\text{YB}_6$  superconducts below 8.4 K, giving it the second-highest critical temperature of known borides, second only to  $\text{MgB}_2$ .  $\text{LaB}_6$  does not superconduct until near-absolute zero temperatures (below 0.45 K), however. Though previous studies have quantified the canonical superconductivity descriptors of  $\text{YB}_6$ 's greater Fermi-level ( $E_F$ ) density of states and higher electron–phonon coupling (EPC), the root of this difference has not been assessed with full detail of the electronic structure. Through chemical bonding, we determine low-lying, unoccupied 4f atomic orbitals in lanthanum to be the key difference between these superconductors. These orbitals, which are not accessible in  $\text{YB}_6$ , hybridize with  $\pi$  B–B bonds and bring this  $\pi$ -system lower in energy than the  $\sigma$  B–B bonds otherwise at  $E_F$ . This inversion of bands is crucial: the optical phonon modes responsible for superconductivity cause the  $\sigma$ -orbitals of  $\text{YB}_6$  to change drastically in overlap, but couple weakly to the  $\pi$ -orbitals of  $\text{LaB}_6$ . These phonons in  $\text{YB}_6$  even access a crossing of electronic states, indicating strong EPC. No such crossing in  $\text{LaB}_6$  is observed. Finally, a supercell (the M k-point) is shown to undergo Peierls-like effects in  $\text{YB}_6$ , introducing additional EPC from both softened acoustic phonons and the same electron-coupled optical modes as in the unit cell. Overall, we find that  $\text{LaB}_6$  and  $\text{YB}_6$  have fundamentally different mechanisms of superconductivity, despite their otherwise near-identity.

superconductivity | chemical bonding | electron–phonon coupling | borides

The massively wide range of physical properties exhibited by rare-earth hexaborides makes them useful for a variety of applications, yet the molecular-level origins of many of these properties are poorly understood. All sharing an ambient crystal structure (Pm3m space group) of a metal surrounded by a network of boron octahedra, these ceramic compounds present themselves vastly differently as semiconductors (1–3), Kondo insulators (4–6), magnetically ordered materials (7, 8), and more (2, 9–15). Lanthanum hexaboride, though primarily exploited in hot cathodes for its high electron emissivity, is also known to be a low-temperature, Bardeen–Cooper–Schrieffer (BCS, i.e., phonon-mediated) superconductor at temperatures below 0.45 K (16). Isostructural yttrium hexaboride, possessing a near-identical phonon spectrum, a similar lattice constant (4.155 Å for  $\text{LaB}_6$ , 4.098 Å for  $\text{YB}_6$ ), and yttrium being one row directly above lanthanum in the periodic table, is a significantly better BCS superconductor at a critical temperature ( $T_c$ ) of up to 8.4 K (17–19). This notably makes it the only reported superconducting hexaboride with a  $T_c$  reachable with  $^4\text{He}$  cryogenics (20, 21). It also possesses the second-highest superconducting  $T_c$  of any metal boride (22), the highest being that of the unusual (23) and thoroughly studied  $\text{MgB}_2$  (24–28), the highest- $T_c$  “conventional” (i.e., phonon-mediated) superconductor.

The canonical descriptions of superconducting phase transitions via Migdal–Eliashberg (29, 30) and McMillan–Allen–Dynes (31, 32) formalisms show density of states (DOS) at the Fermi level ( $E_F$ ) and electron–phonon coupling (EPC) to be the two key factors contributing to superconducting temperature, as both are descriptors for how drastically electrons in a superconductor “feel” the lattice and thus form Cooper pairs. As  $E_F$ -DOS and EPC increase, so too will  $T_c$ . Indeed, samples of  $\text{YB}_6$  of increasing  $T_c$  have been confirmed by  $^{89}\text{Y}$  nuclear magnetic resonance (NMR) to also have increasing  $E_F$ -DOS, and  $\text{YB}_6$  is known through tunneling and DC magnetization (33), point-contact spectroscopy (34), and electronic Raman scattering (35), as well as Density functional theory (DFT) (36), to have moderate to strong EPC, depending on the sample.

While experimental and computational studies have been conducted to characterize the Fermi level electronic structure (3, 12, 37–41) of  $\text{YB}_6$  and  $\text{LaB}_6$  and their phonon modes (41–48) contributing to EPC, the linkage of the two—how frontier electronic eigenstates physically couple to these lattice vibrations—has yet to be established, as has been done with other prominent phonon-mediated superconductors (26, 27, 49). Prior

## Significance

Chemical bonding is a powerful approach to materials rationalization and design due to its beauty in simplicity. As the field of quantum materials takes the scientific community by storm, an understanding of these materials (such as superconductors) in the language of chemistry is essential for complete characterization and predictive capabilities. In this work, we demonstrate such an understanding by differentiating, using only their molecular orbitals and vibrational modes, two superconductors which are expected to behave identically but are drastically different in reality. This study paves the way for a chemist's view of phonon-mediated superconductivity and opens the door to prediction of other quantum materials' behavior using chemical bonding.

Author affiliations: <sup>a</sup>Department of Chemistry and Biochemistry, University of California, Los Angeles, CA 90095; <sup>b</sup>Departamento de Química Física and Instituto de Biocomputación y Física de Sistemas Complejos, Universidad de Zaragoza, Zaragoza 50009, Spain; <sup>c</sup>Departamento de Física, Facultad de Ciencias, Universidad de Chile, Santiago 7800024, Chile; <sup>d</sup>Center for the Development of Nanoscience and Nanotechnology, Santiago 9330111, Chile; <sup>e</sup>Department of Materials Science and Engineering, University of California, Los Angeles, CA 90095; and <sup>f</sup>California NanoSystems Institute, University of California, Los Angeles, CA 90095

Author contributions: R.H.L., J.M., F.M., and A.N.A. designed research; R.H.L., J.M., C.E.D., and F.M. performed research; R.H.L., J.M., F.M., and A.N.A. analyzed data; and R.H.L., F.M., and A.N.A. wrote the paper.

The authors declare no competing interest.

This article is a PNAS Direct Submission.

Copyright © 2024 the Author(s). Published by PNAS. This article is distributed under Creative Commons Attribution-NonCommercial-NoDerivatives License 4.0 (CC BY-NC-ND).

<sup>1</sup>To whom correspondence may be addressed. Email: fvmunoz@gmail.com or ana@chem.ucla.edu.

This article contains supporting information online at <https://www.pnas.org/lookup/suppl/doi:10.1073/pnas.2316101121/-DCSupplemental>.

Published March 28, 2024.

studies of our group have quantitatively and qualitatively explained properties of metal hexaborides through the lens of chemical bonding (6, 9, 50), and in this study, we extend this capability to superconducting hexaborides by analyzing changes in this bonding under phonon-induced lattice deformations.

## Results

**Determination of the Phonon Modes Responsible for Superconductivity.** The BCS theory of superconductivity attributes the formation of Cooper pairs to lattice vibrations (phonons) pairing electrons near a material's Fermi level ( $E_F$ ), ultimately forming a condensate of Cooper pairs and thus an electron flow experiencing zero resistance. In turn, the phonon modes that will form Cooper pairs by inducing a large EPC are likely those breaking the degeneracy of partially occupied electron bands at the Fermi level (51). While a number of modes in the phonon dispersion of  $\text{YB}_6$  (Fig. 1A) and  $\text{LaB}_6$  (Fig. 1B) can accomplish this (SI Appendix, Fig. S1 shows the effects of all 21 phonons on the electronic band structures), the modes of interest in this group are those possessing the lowest frequency, as they are likely to require the least amount of vibrational energy to break degeneracy. These flat phonon bands, circled in red at the  $\Gamma$  (G) points of Fig. 1, represent a Raman-active  $T_{2g}$  mode which is triply degenerate as the same motion in the x, y, and z directions of the lattice. Of the 21 phonons, they are the 13th to 15th lowest in energy (the order of the three is arbitrary) at approximately 21 THz. Fig. 1C shows a visualization of each of these vibrations (labeled i, ii, and iii) while Fig. 1D and E show how each breaks electronic degeneracy in  $\text{YB}_6$  and  $\text{LaB}_6$ . The other, higher-energy group of phonons which can be responsible for Cooper pairs are at 35 to 40 THz for  $\text{YB}_6$  and 32 to 36 THz for  $\text{LaB}_6$  (phonons 19 to 21). Although the BCS model of superconductivity allows virtual phonons (i.e., phonons too high in energy to be “occupied” vibrational quasiparticle bands) to participate in Cooper pairing, these three modes break band structure degeneracies in a near-identical manner to the phonons in Fig. 1C and are thus omitted from the remainder of this study.

All six phonons mentioned here, 13 to 15 and 19 to 21, can be visualized with an animation-like representation using the GIF or interactive files attached as SI. All six involve motion of the boron atoms only, with the metal remaining stationary. In contrast to the low-energy vibrations of the metal in the boron “cage,” these sets of mid and high-energy phonons are confirmed by experimental Raman scattering of  $\text{LaB}_6$  and  $\text{YB}_6$  to exhibit little to no anharmonicity, as shown by their Gruneisen parameters. This same study determines EPC contributions of the anharmonic, acoustic phonons to be low and observes opposite temperature dependence of boron octahedra vibrations between  $\text{YB}_6$  and  $\text{LaB}_6$ , hypothesizing that these higher-frequency, optical phonons promote a higher  $T_c$  in  $\text{YB}_6$  (48). This is consistent with our computational observation of phonons 13 to 15 and 19 to 21 being significant for superconductivity in these two materials.

The magnitude of displacement along the phonon mode in Fig. 1D and E is arbitrary and meant only to demonstrate degeneracy breaking, but it should be noted that at such low temperatures as 8.4 or 0.45 K, the only appreciable vibrational energy contributing to these displacements comes from zero-point energy (ZPE):  $\frac{1}{2} \hbar\omega_{\text{phonon}}$ , which corresponds to 0.04215 eV and 0.0434 eV, for  $\text{YB}_6$  and  $\text{LaB}_6$ , respectively. SI Appendix, Fig. S2, by plotting the ZPE line and DFT energies along the phonon distortion, shows that the classical turning points past which the lattice cannot distort are approximately 1.5 to 2.2 degrees for  $\text{YB}_6$  and 1 to 3 degrees for  $\text{LaB}_6$ , depending on the phonon. This angle is shown

at the *Bottom of SI Appendix, Fig. S2* (labeled  $\phi$ ) and is given as a range because the symmetry of some of the frontier electronic bands prevents the EPC from being completely isotropic in x, y, and z directions, as discussed in the coming section. This ZPE analysis will become essential information in later discussion of chemical bonding under phonons, as  $\text{YB}_6$  undergoes a crossing of states along the phonon-induced potential energy surface (PES) at a deformation angle of approximately 2 degrees, while  $\text{LaB}_6$  experiences no such crossing, even up to unphysical 5 degree distortions (Fig. 3B).

**Relation of Frontier Orbitals between  $\text{YB}_6$  and  $\text{LaB}_6$ .** Fig. 1C and D demonstrate that the lattice vibrations relevant to superconductivity are “rocking” motions of the two boron atoms fusing  $\text{B}_6$  octahedra. Our previous studies showed that these B–B bonds constitute the most significant B–B interactions in rare-earth hexaborides (6, 9). We aim to reveal how the eigenstates (orbitals) comprising the valence bands of the studied hexaborides physically couple to these vibrations. From the PDOS in Fig. 1D and E, we see that boron 2s and 2p orbitals and yttrium 4d orbitals comprise the Fermi surface of  $\text{YB}_6$ , while boron 2s and 2p orbitals and lanthanum 5f orbitals comprise that of  $\text{LaB}_6$ . Specifically, in both materials, all boron valence AOs (i.e., of principal quantum number 2) contribute, with additions of  $4d_x^2$ ,  $4d_y^2$ , and  $4d_z^2$  AOs in  $\text{YB}_6$  and  $4f_{xz}^{3/2}$ ,  $4f_{yz}^{1/2}$ ,  $4f_{xz}^{1/2}$ ,  $4f_{zx}^{1/2}$ , and  $4f_z^3$  AOs in  $\text{LaB}_6$ . In atomic lanthanum, no electrons occupy 4f orbitals and thus it is somewhat surprising to see these states occupying  $\text{LaB}_6$ 's  $E_F$  rather than 6s or 5d. 4f orbitals, however, have been shown to enable covalency with very compact valence orbitals of boron (52). In addition, 4f AOs are bond-promiscuous in a solid because unlike 5d and 6s, which possess two and six nodes in their radial wavefunctions, they have no radial nodes and are thus not destabilized by the “chemical pressure” of a fixed lattice. By contrast, orbitals with radial nodes would begin to experience destructive interference when pushed together due to a sign change in wavefunction phase. For this reason, significant 4f contributions have been shown to dominate the  $E_F$ -DOS even at extreme pressures for the proposed high- $T_c$  superconductor  $\text{LaH}_{10}$  (53). A more canonical example of this nodality phenomenon is solid beryllium being held together by hybridized 2p orbitals despite a single Be atom having only 2s valence electrons (2s orbitals have radial nodes but 2p do not) (54, 55).

In Fig. 2, we show the Kohn–Sham orbitals of our DFT calculations for each valence and conduction band, plotted specifically at the  $\Gamma$  point such that all unit cells' orbitals are in-phase. Unrotated Bloch orbitals, rather than Wannier functions, are plotted for their ability to describe the delocalized bonding of the metallic bulk. We henceforth refer to these orbitals in the chemistry vocabulary of highest occupied molecular orbitals (HOMO) for the valence bands and lowest unoccupied molecular orbitals (LUMO) for the conduction bands, HOMO and LUMO referred to collectively as frontier orbitals. It is valid in our study to analyze these bands at the  $\Gamma$  point due to the electron–phonon coupling being localized near the  $\Gamma$  point when plotted along the phonon dispersion. SI Appendix, Fig. S3 shows there is one other source of significant EPC coming from these same phonon bands at momentum M, which we discuss via Fermi surface analysis in the section “Additional EPC in a supercell.” The bonding picture at M is similar to that at  $\Gamma$ , but phase relations between unit cells must be considered.

$\text{YB}_6$  has two degenerate valence bands and three degenerate conduction bands at and around the  $\Gamma$  point, while  $\text{LaB}_6$  has the opposite degeneracies. Quite notably, the HOMO of  $\text{YB}_6$  looks identical to the LUMO of  $\text{LaB}_6$ . Both sets of orbitals are a system

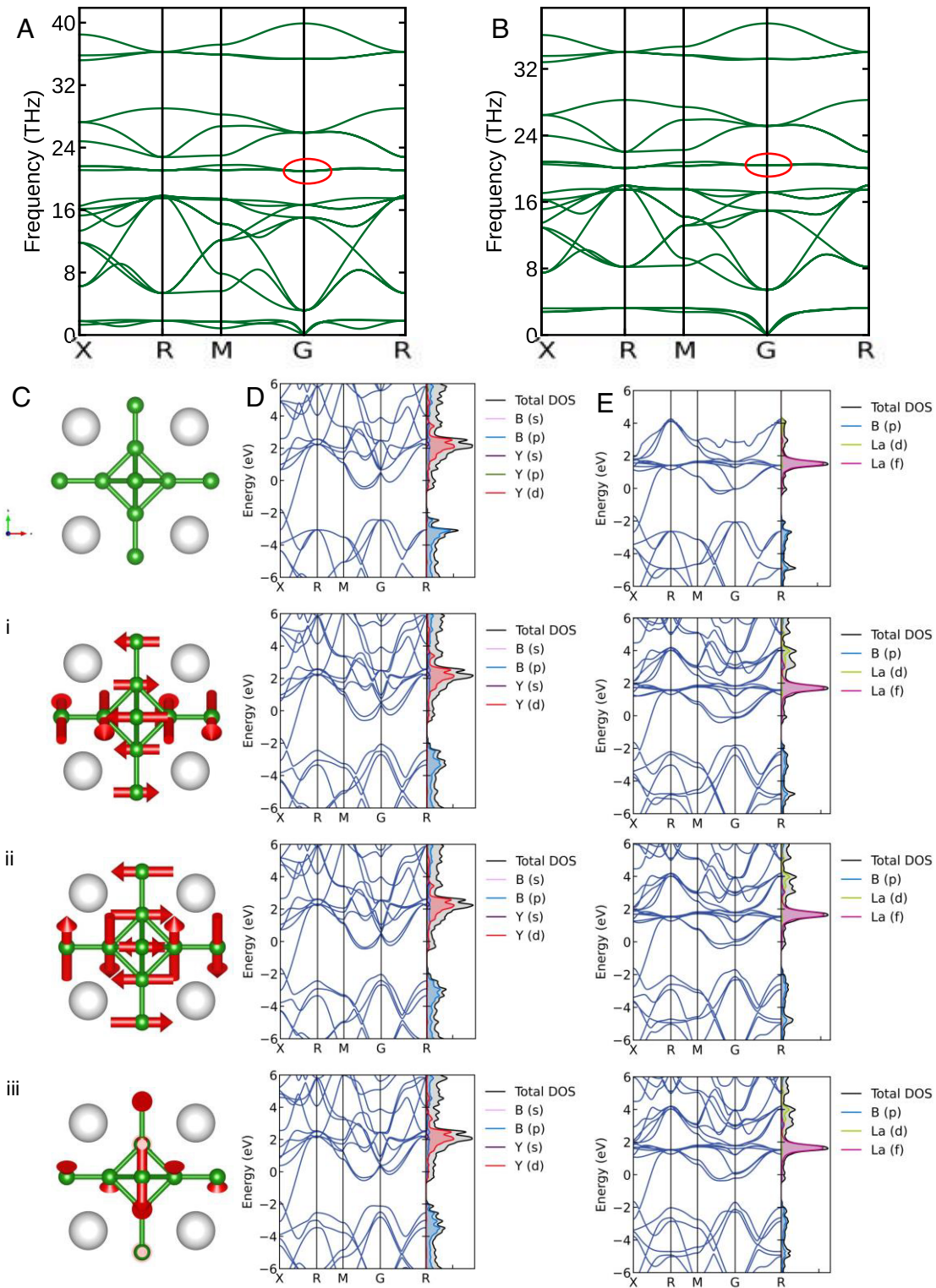


**Fig. 1.** Phonon dispersions of  $\text{YB}_6$  (A) and  $\text{LaB}_6$  (B). (C) Visualizations of the lowest energy phonons responsible for superconductivity at the  $\Gamma$  point in  $\text{YB}_6$  and  $\text{LaB}_6$ ; phonons 13 to 15. White atoms represent the metal (yttrium or lanthanum); green atoms are boron. The topmost structure, with no phonon mode arrows, represents the equilibrium geometry. (D) Effect of the three phonons applied to  $\text{YB}_6$  on degeneracy splittings at the Fermi level. (E) Effect of the three phonons applied to  $\text{LaB}_6$  on degeneracy splittings at the Fermi level.

of metal-metal and B-B  $\sigma$ -bonds extending along the x, y, and z lattice vectors of the unit cell. They are doubly, rather than triply degenerate, however, due to the  $d_z^2$  and  $d_{x^2-y^2}^2$  AOs forming the metal–metal bond possessing  $E_g$  symmetry. Additionally, the LUMO of  $\text{YB}_6$  looks identical to the triply degenerate HOMO

of  $\text{LaB}_6$ , absent bonding involvement of the metal in  $\text{YB}_6$ . This is a system of  $\pi$ -bonds on octahedra-fusing boron dimers which link unit cells, and in the case of  $\text{LaB}_6$  HOMO, 4f electron density hybridizes with this  $\pi$  system as well. Greater in-phase overlap of molecular orbitals lowers their energy, and thus it can be readily

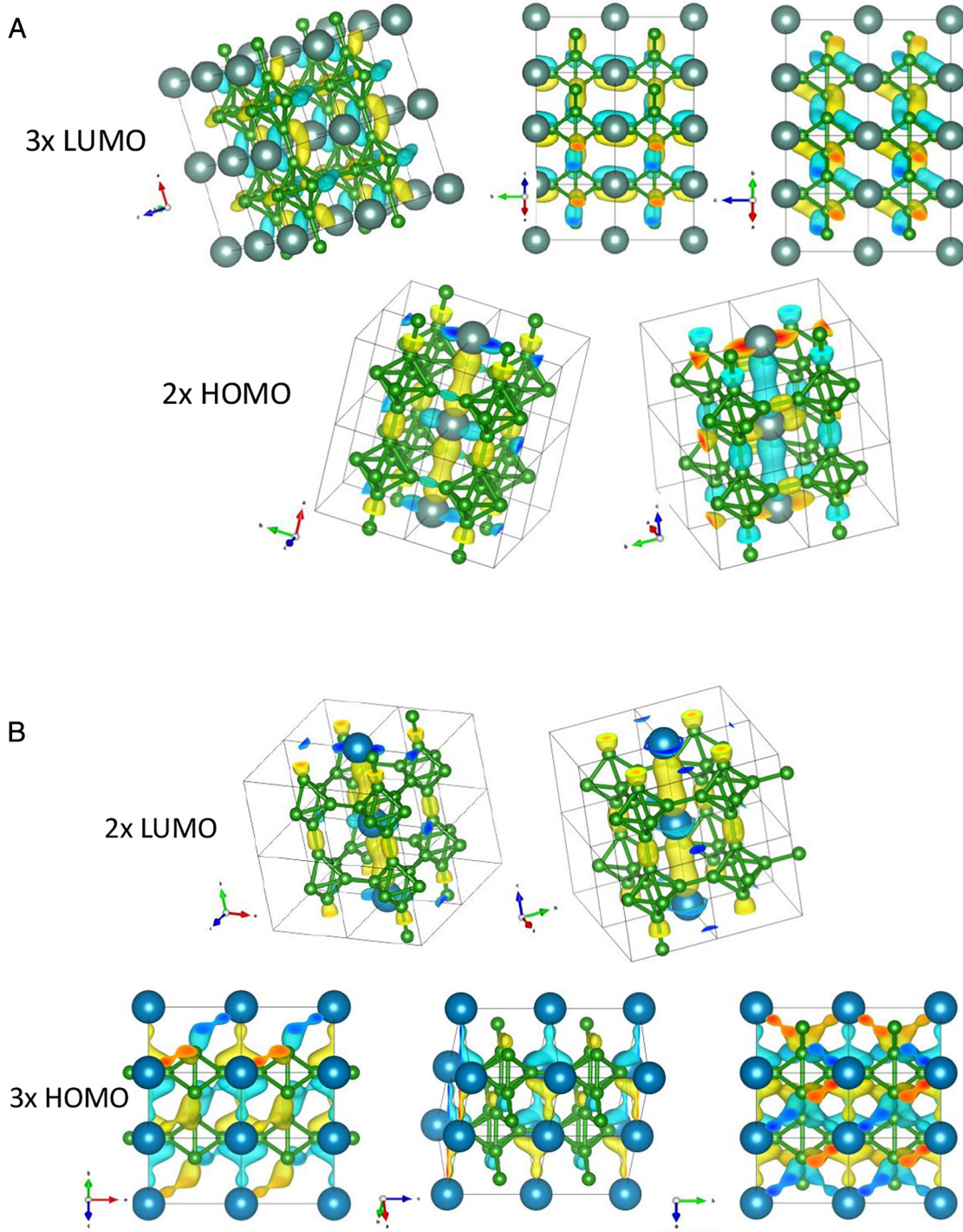


**Fig. 2.** Frontier orbitals of  $\text{YB}_6$  (*A*) and  $\text{LaB}_6$  (*B*). For each material, HOMO are shown in the *Lower* row and LUMO in the *Upper* row. Gray atoms are yttrium, blue atoms are lanthanum, and green atoms are boron. Isovalues were chosen to show the bonds reflected in the PDOS and are approximately 0.03 for  $\sigma$ -bonds and 0.15 for  $\pi$ -bonds. Due to the difference in localized  $\sigma$ -bonds versus delocalized  $\pi$ -bonds, the same isovalue could not be used for both. Lattice vectors are shown to the left of each orbital and the degeneracy is shown by 2 $\times$  or 3 $\times$  on the HOMO/LUMO label.

deduced that this inversion of valence and conduction bands between  $\text{LaB}_6$  and  $\text{YB}_6$  is due to the participation of the 4f orbitals, which are unoccupied but low-lying in lanthanum's  $[\text{Xe}]5\text{d}^16\text{s}^2$  electron configuration, yet completely inaccessible in ground-state yttrium ( $[\text{Kr}]4\text{d}^15\text{s}^2$ ).

**Density of States Comparison at the Fermi Level.** From the electronic band diagrams in Fig. 1 *D* and *E*, it can be clearly determined that  $\text{YB}_6$  has a significantly larger DOS at the Fermi level than  $\text{LaB}_6$ , making this DOS contribution to the

McMillan–Allen–Dynes (MAD) description straightforward. While only two bands comprise the Fermi surface of  $\text{YB}_6$ , they cross  $E_F$  six times. Three bands comprise  $\text{LaB}_6$ 's Fermi surface, but all come together in degeneracy at the  $\Gamma$  point with two crossing  $E_F$  at only one other point and the third not at all, for a total of only three crossings of the Fermi level. All these bands have significant curvature (“band width”) at and near  $E_F$  (i.e., they are not at all flat), so their contributions to the  $E_F$ -DOS occur only due to point intersections with the Fermi level. In  $\text{YB}_6$ , it has been established (15) that the finite states at  $E_F$  indicate metallic bonding. By contrast,

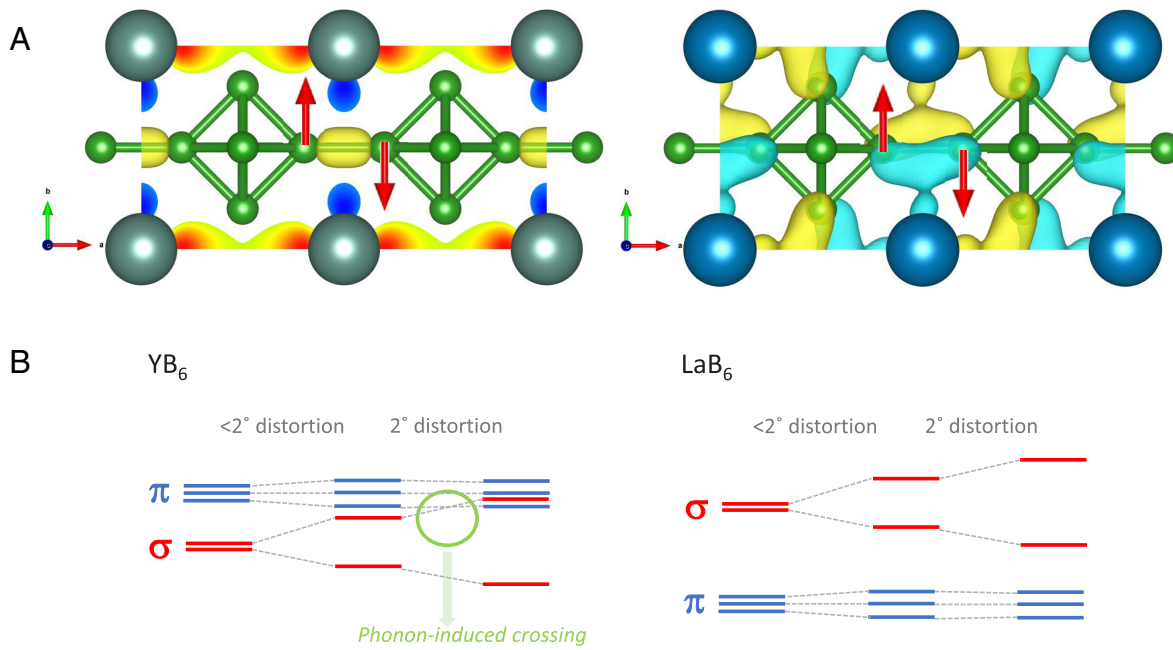


**Fig. 3.** (A) One of two  $\text{YB}_6$  (Left) and  $\text{LaB}_6$  (Right) HOMO, showing how their shapes lead to more ( $\text{YB}_6$ ) or less ( $\text{LaB}_6$ ) EPC. (B) Qualitative picture of orbital degeneracy breaking with the frozen phonon in  $\text{YB}_6$  (Left) and  $\text{LaB}_6$  (Right), noting the ZPE-accessible crossing in  $\text{YB}_6$ .

$\text{LaB}_6$  exhibits essential metal–boron covalency at  $E_f$  in the  $\pi$ -system, contributing to a smaller  $E_f$ -DOS than that of the isolated Y–Y and B–B  $\sigma$  bonds we observe at the  $E_f$  of  $\text{YB}_6$ .

## Discussion

**Coupling of  $T_{2g}$  Phonons to HOMO of Each Material.** Now that the frontier orbitals of  $\text{YB}_6$  and  $\text{LaB}_6$  have been identified, we can begin to discuss how their bonding character leads to a large electron–phonon coupling, i.e., involving splitting of their degeneracies at  $E_f$ . In both materials, phonons 13 to 15 rock inter-octahedron  $\text{B}_2$  units back and forth like a “see-saw” (Fig. 1C and GIF and interactive files for reference have been provided in *SI Appendix*). As mentioned, in  $\text{YB}_6$ , these  $\text{B}_2$  units are held together by a  $\sigma$ -bond formed by  $p_z$ -AOs, and do not engage with the metal or other B atoms at  $E_f$ . The rocking phonon is applied, the  $p_z$  orbitals go out of  $\sigma$ -alignment, and the  $\sigma$ -overlap worsens. This is shown on the *Left* of Fig. 3A.

By contrast,  $E_f$  in  $\text{LaB}_6$  is comprised of  $\pi$ -bonds on  $\text{B}_2$  units which overlap with La’s 4f orbitals at the phonon’s axis of rotation, making these bonding orbitals see-saw shaped themselves. When the  $\text{B}_2$  unit is rocked by the phonon, the electron density between La and the center of  $\text{B}_2$  is merely a “fulcrum” for this rocking, and the  $\text{B}_2$  itself remains  $\pi$ -bonded off the bond axis with no phonon-induced misalignment of the B  $p_{xy}$ -AOs. Thus, overlap is largely unaffected by the phonon and EPC is expected to be quite low. This can be visualized on the *Right* side of Fig. 3A. Recalling that the HOMO and the phonon are triply degenerate for  $\text{LaB}_6$ , we note that the other two phonons which do not align with the  $\text{LaB}_2$  see-saw unit can still couple to it. Having only ~2/3 of the electron–phonon interactions per phonon, however,  $\text{LaB}_6$  will have significantly less EPC than  $\text{YB}_6$ , in which each component of the triply degenerate HOMO couples to all three components of the phonon. This qualitatively explains  $\text{YB}_6$  being the superior BCS superconductor with a much higher critical temperature.

In order to assess this hypothesis rigorously, we began to examine frontier orbitals after the frozen phonons were applied and uncovered something quite striking. The mildly distorted structures resulting

from frozen phonons retain largely the shapes of their HOMO and LUMO, and unsurprisingly, degeneracies of these orbitals break according to which phonon direction couples to their overlap. At a phonon distortion of approximately 2 degrees (accessible by ZPE, as shown in *SI Appendix*, Fig. S2), however, one of the  $\pi$ -bands of  $\text{YB}_6$  drops in energy, switches with one of the  $\sigma$ -bands, and becomes occupied at  $\Gamma$  (Fig. 3B). The process that occurs is, naturally, identical in all three Cartesian directions. Application of the phonon changes point group symmetry from  $O_h$  ( $\text{Pm}3\text{m}$ ) to  $C_i$ , within which the  $\pi$ -system is of  $a_u$  symmetry, and the  $\sigma$ -system is  $a_g$ . Thus, the state crossing is not a conical intersection by the no-crossing theorem. Its presence, however, is nonetheless proof of major phonon-induced changes in electronic structure and indicative of strong EPC. No such crossing occurs in  $\text{LaB}_6$  at any deformation angle computed, ZPE accessible or otherwise (Bottom of Fig. 3B).

**Additional EPC in a Supercell.** *SI Appendix*, Fig. S3 shows that in addition to the  $\Gamma$  point, significant EPC stems from the M point of the Brillouin zone (BZ) where all unit cells are fully out of phase with their neighbors in all three Cartesian directions. Indeed, Fig. 1 B and E show electronic band degeneracy splitting at M at the Fermi level. It is essential to understand how the mechanism of EPC present at  $\Gamma$  extends to the M point and does not extend to other points of high symmetry. We perform DFT calculations of  $2 \times 2 \times 2$  supercells with the frozen phonon applied with the unit cell phase relations of M, X, and R and analyze the effect on the Fermi surface (FS). For the M point of interest, *SI Appendix*, Fig. S4 shows slices of the FS cut along the (001) plane at various values of  $k_z$ . Comparing  $\text{YB}_6$  and  $\text{LaB}_6$ , the differences are minimal, with exception of phonon 15 around  $k_z = 0.4$ . The changes on this slice are much larger for  $\text{YB}_6$ .

Fig. 4 A and B show the unperturbed Fermi surface of  $\text{YB}_6$  (no supercell) for two values of  $k_z$ . The red curves show the band folding of these slices into a  $2 \times 2 \times 1$  supercell (for the sake of simplicity, the folding along  $k_z$  is ignored). The folded BZ is the dashed box. The folding induces new degeneracies, or Fermi nesting, on the folded BZ. These points and their position in the original BZ are marked by green points, which an arrow going from  $\Gamma$  to M connects in the original BZ.

This arrow's direction coincides with the phonon with the largest EPC, causing a sizable Fermi nesting. Fig. 4C shows the actual FS of a  $2 \times 2 \times 2$  supercell of  $\text{YB}_6$ , with  $k'_z = 0.4$  (in the folded BZ). Again, the bands of interest are in red. The other bands come from the folding along  $k_z$  and are of no interest here. Fig. 4D shows the previous FS of Fig. 4C, but under the effect of frozen phonon 15 with modest amplitude. We readily see that these new degeneracies introduced by the supercell band folding are broken by the phonon. By symmetry, the same phenomenon occurs for phonons 13 and 14, along the (100) and (010) planes, respectively.

To address why this nesting implies a large EPC specifically at (and near) the M point, and why it is more drastic in  $\text{YB}_6$  than in  $\text{LaB}_6$ , we consider the phonon's effect on the boron octahedral cage around the metals in each supercell. At X and R, the application of the frozen phonon breaks lattice  $O_h$  symmetry, but each metal atom has the same surrounding boron geometry (Fig. 5A, noting that the unit cells are related by inversion symmetry at X but still give the same surroundings of the metal). At the M point, however, two different sizes of the boron cage are introduced with the phonon, emphasized with black squares, giving the lattice twice the periodicity as at equilibrium before. This effect, known as a dimerization, is well studied in other, quasi-1-dimensional (1-D) materials in the context of Peierls distortions (56, 57), which cause periodic fluctuations in electron density known as charge density waves (CDW) (58).

The Peierls mechanism involves the splitting of a degeneracy in a metallic system, lowering its energy at the same time the distortion increases the energy. In 1-D systems, this mechanism is energetically favorable for a finite distortion. But, in general, it is not the case for 3D crystals such as  $\text{YB}_6$  and  $\text{LaB}_6$ . Nevertheless, a Peierls-like distortion or dimerization is very effective for lifting a degeneracy in a quasi-1D band, and a large EPC is expected from it.

Note S1 gives a full explanation of a tight binding (TB) model in the context of  $\text{YB}_6$  and  $\text{LaB}_6$ , but what is most important when comparing the two materials is the “1D-ness” of their valence bands. It is straightforward to identify a quasi-1-D chain in  $\text{YB}_6$  as the Y-Y  $\sigma$  bonds run parallel to the prominent B-B  $\sigma$ -bonds (Fig. 5b). When the phonon acts at M, Y atoms obtain twice the period in this chain direction and a splitting of degeneracies should appear, explaining the large changes obtained by the frozen phonon 15 in *SI Appendix, Fig. S4*. On the other hand, the most 1-D-like periodicity of  $\text{LaB}_6$ 's HOMO is a  $45^\circ$  lattice rotation from that of  $\text{YB}_6$ 's and the boron octahedra become part of the “chain.” This makes the band “less 1-D,” and a dimerization in  $\text{LaB}_6$  should not be as effective as in  $\text{YB}_6$  to split degeneracies. In the context of the TB model, the La atoms and the octahedra will have very different on-site terms, leaving just one TB band close to the Fermi level. This band in  $\text{LaB}_6$  experiences a weaker Peierls-like effect since the other dimensions are unaffected by the dimerization (indeed, there is still nonzero EPC at M), but  $\text{YB}_6$

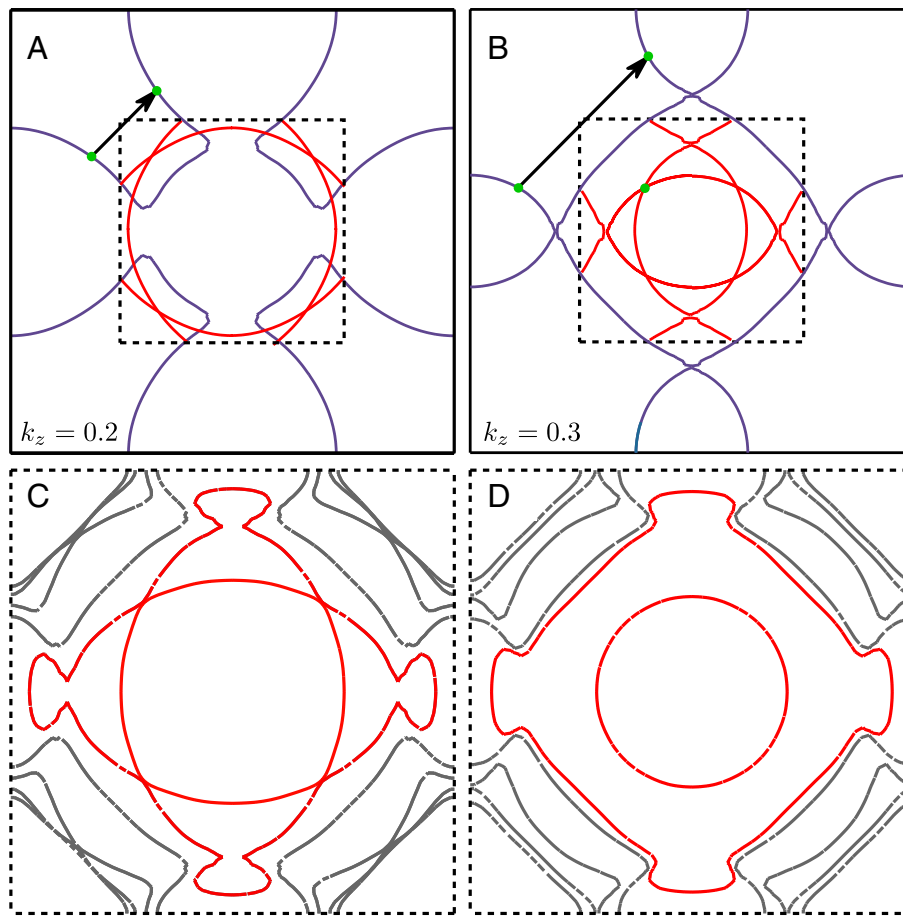


**Fig. 4.** (A) Equilibrium  $\text{YB}_6$  FS at  $k_z = 0.2$ . Blue lines show the unit cell FS slice, solid black lines show the (001) plane of the unit cell BZ, dotted black lines show the (001) plane of a  $2 \times 2 \times 1$  supercell BZ. Green points denote sites where Fermi nesting occurs with the band folding. An arrow denotes the direction of the path between  $\Gamma$  and M. Bands of interest due to nesting in the (001) plane are in red. (B) Equilibrium  $\text{YB}_6$  FS at  $k_z = 0.3$ , using the same symbols and coloring as (A). (C) FS at  $k_z = 0.4$  of a  $2 \times 2 \times 2$  supercell at equilibrium. (D) FS at  $k'_z = 0.4$  of a  $2 \times 2 \times 2$  supercell with frozen phonon 15 applied, showing that the red bands of interest now have broken degeneracies. The extra bands in gray are due to the folding in  $k_z$ .

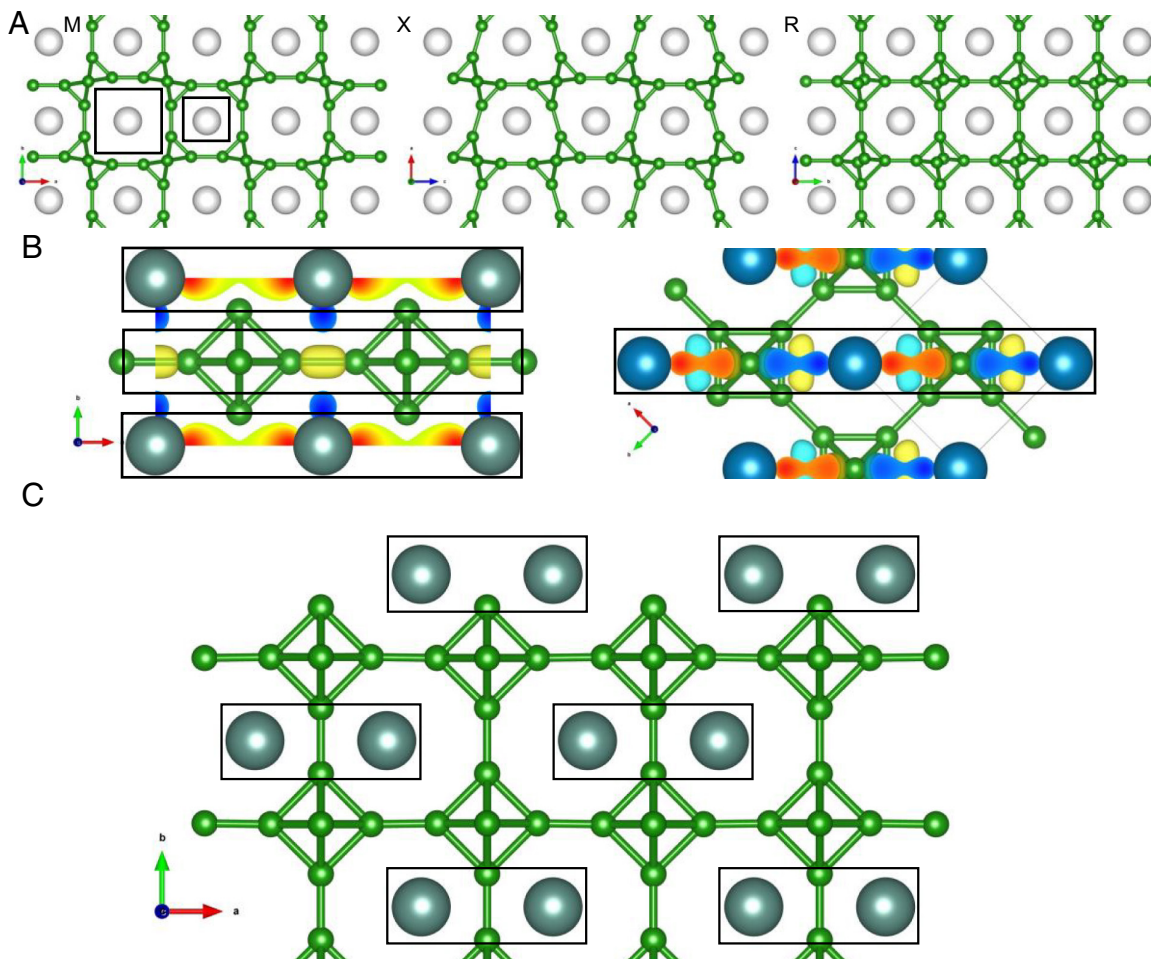


**Fig. 5.** (A) Frozen phonon applied to the supercell at the M (Left), X (Middle), and R (Right) points. White atoms can be either Y or La. Green atoms are boron. Black squares emphasize the difference in surroundings of the metal at the M point. (B) 1-D “chains” formable by the valence bands of YB<sub>6</sub> (Left) and LaB<sub>6</sub> (Right). Chains are noted with black rectangles. Y atoms are gray, La atoms are blue, and B atoms are green. (C) Dimerization of the YB<sub>6</sub> lattice under a softened, acoustic phonon, with dimers boxed in black. Comparison to (B) shows this occurs in the same direction of one of the Y–Y σ-bonds, creating EPC in the form of a Peierls-like effect. Y atoms are gray, and B atoms are green.

is decidedly the “more 1-D” of the two materials, explaining the higher EPC and T<sub>c</sub>.

While some experimental studies predict EPC of acoustic phonons to be low in both these materials (48), others attribute a great deal of YB<sub>6</sub>’s higher T<sub>c</sub> to these phonons (22). Phonons with very low frequency are likely to be highly anharmonic, so the approximations used in EPC calculations (*SI Appendix*, Fig. S3) are unlikely to provide useful information. Thus, we rely only on frozen phonon calculations here. It can be readily seen from Fig. 1 *A* and *B* that the three lowest of these phonons soften for YB<sub>6</sub>, but not LaB<sub>6</sub>. Thus, for YB<sub>6</sub>, a small perturbation (changes in temperature, pressure, etc.) can turn the frequency of the acoustic phonons negative, triggering a change of equilibrium geometry. This difference in phonon spectrum has been attributed to the slightly larger atomic radius of lanthanum leaving less space in the boron cage for the metal atom to “rattle” along the acoustic phonon modes (45).

Indeed, we observe large changes in the Fermi surface for YB<sub>6</sub> due to two of the frozen acoustic phonons at M (phonons 2 and 3), but little to no observable change for LaB<sub>6</sub> (*SI Appendix*, Fig. S4). Once again, this is readily explained by bonding at E<sub>f</sub>. In the case of YB<sub>6</sub>, a totally symmetric mode at the Γ point will not affect the d–d bonding of Y atoms, but within other supercells, σ overlap will be strongly affected by movement of Y out of phase

between unit cells, much like the rocking modes 13 to 15 affecting σ-overlap between boron atoms. LaB<sub>6</sub>, however, has no such metal–metal bonding, so no such EPC arises from the acoustic phonons. The vast majority of the LaB<sub>6</sub> electron density at E<sub>f</sub> is on the unaffected boron octahedra for LaB<sub>6</sub>, and thus EPC is low.

From another viewpoint, phonon softening is a main signature of a Peierls distortion (56), and we thus consider these two acoustic phonons in the context of dimerization. Fig. 5C shows the resulting geometry when one of the two frozen phonons is applied, and along only one axis (the same axis a Y–Y σ bond runs along), a clear dimerization occurs between the Y atoms. The other frozen phonon gives the same result, but along a different axis with the other σ bond. The third acoustic phonon, which further dips at M and along the Γ–R path, acts along the final axis, which has no σ bonding. Indeed, Lortz et al find a large EPC peak for YB<sub>6</sub> at 8 meV but a much smaller one at 4.5 eV (22), in good agreement with the computed frequencies at M: 7 meV for phonons 2 and 3 and 3.6 meV for phonon 1.

Given that the Y atoms are σ-bonded along a single direction per Bloch state at E<sub>f</sub>, the effect of the acoustic phonons is much closer to the “textbook” example of a 1-D chain of hydrogen atoms than the previous Peierls argument of phonons 13 to 15. Though competition of other relevant phonons in a 3-D lattice prevents an actual CDW, this dynamical Peierls effect is more “traditional”

than that of phonons 13 to 15 in that the tight-binding hopping strength is modified, rather than the on-site energy. This is again discussed in detail in *SI Appendix, Note S1*. In summary, we observe two ways to induce a Peierls-like distortion in  $\text{YB}_6$ , from low-energy and high-energy phonons.

**Effects of Isotropic Pressure and Stretching.** The effects of strain and pressure are essential in studying bonding-governed properties of materials (59–61): hexaborides (7, 62–66) or otherwise. Specifically in the case of hexaboride superconductors, the effects of isotropic pressure have been thoroughly studied experimentally and computationally (36, 42, 43, 48), including in the context of phase transitions out of the  $\text{Pm}3\text{m}$  space group (39, 41). Experimentally, pressure has been shown to lower the superconducting transition of  $\text{YB}_6$  (43), and this has been attributed to hardening of the lowest-energy, acoustic phonon modes, a “rattling” of Y in the boron cage which Xu et al. computationally deem responsible for superconductivity (45). Our calculations of k-point and band-resolved phonon linewidths and frozen phonons’ effects on electronic band structure, however, show these phonons to contribute only partially to EPC, along with phonons 13 to 15 and 19 to 21 involving the bridging boron atoms between octahedra.

As shown in Fig. 6, we find that computed band structures with applied pressure slightly expand the gap between valence and conduction bands, though both materials remain metals. We compute pressures up to 112 kbar in order to match experiment (43). Though phonon dispersion and EPC calculations at a variety of pressures are computationally prohibitive, the same argument of phonon hardening/constriction with compression can be made qualitatively. The widening of the energy difference between valence and conduction bands has to do with the change in AO-overlap upon compression: antibonding states will always rise in energy, and the bonding states may rise or drop, depending on the bond length imposed by the lattice, compared to the optimum for the given pair of atoms (60). The shifts are more pronounced for the  $\sigma$ -bonds, i.e., HOMO of  $\text{YB}_6$  and LUMO of  $\text{LaB}_6$ , than for  $\pi$ -bonds that have weaker AO-overlaps. These shifts in band energies will affect the extent to which phonons 13 to 15 and 19 to 21 can interact with them (60). This is a question for future study.

Particularly for the case of  $\text{LaB}_6$ , where localized f-orbitals are the cause of its deviation from  $\text{YB}_6$ , the question is begged whether stretching these materials isotropically could have the opposite effect of applied pressure: increasing  $T_c$ . If the boron  $\pi$  system becomes so far removed from La that the 4f interaction can no

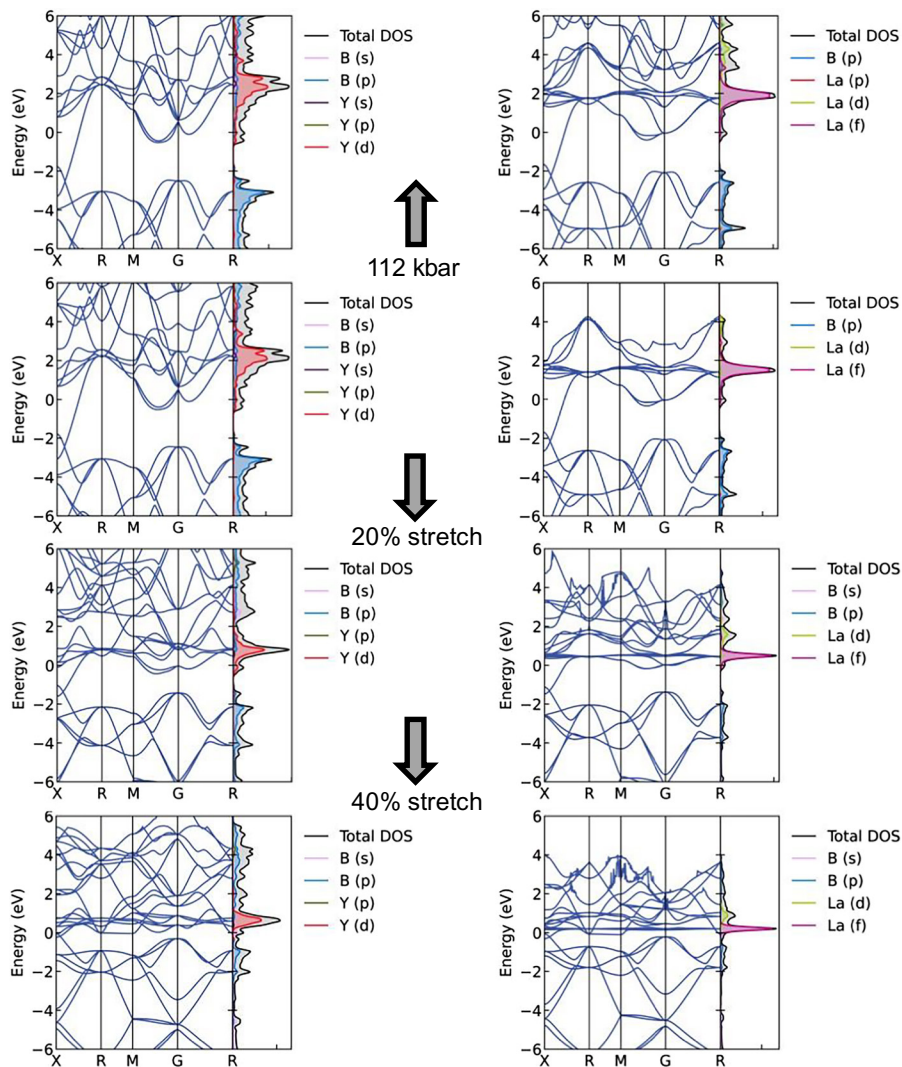


**Fig. 6.** Effects of pressure and isotropic stretching on the electronic band structures of  $\text{YB}_6$  (Left) and  $\text{LaB}_6$  (Right). The percent stretching indicates that each of the three lattice vectors was stretched by the given percentage.

longer stabilize it, the valence and conduction bands could theoretically swap in energy order and a band structure similar to  $\text{YB}_6$  could be observed. As demonstrated in Fig. 6, the equilibrium valence and conduction bands can be made degenerate in  $\text{LaB}_6$  but never to flip. As before, this effect is less pronounced in the  $\pi$  bands than the  $\sigma$  bands. Furthermore, this degeneracy occurs at extreme bond stretching lengths (1.4 times the equilibrium lattice vector of 4.155 Å for  $\text{LaB}_6$  and 4.098 Å for  $\text{YB}_6$ ) at which, in reality, the material would almost certainly experience mechanical failure. For context, based on their thermal expansion coefficients, a bond stretch of 1.6% length corresponds to a heating of approximately 2,000 °C (67). Furthermore, static electron correlation dramatically increases at stretched bond lengths near and past the Coulson-Fischer point, which can make DFT predictions incorrect. The question of whether anisotropic expansion of the lattice, by chemical doping or mechanical stress, can produce this desired effect in  $\text{LaB}_6$  may be addressed in a future study.

**Conclusions.** Lanthanum and yttrium hexaboride have been shown in this study to superconduct by different electron–phonon coupling mechanisms as governed by their chemical bonding and the phonons we show responsible for superconductivity.  $\text{LaB}_6$ , a relatively unextraordinary superconductor at  $T_c = 0.45$  K, has a Fermi level ( $E_F$ ) comprised of B–B  $\pi$  bonds overlapping with 4f orbitals of La. This see-saw shaped bonding of the HOMO aligns with the  $\text{B}_2$  rocking motion of the main, triply degenerate phonon responsible for superconductivity, leading to less electron–phonon coupling.  $\text{YB}_6$ , the second-highest  $T_c$  superconductor of the metal borides at 8.4 K, is remarkably different from its La counterpart. Due to the unavailability of f orbitals for bonding stabilization, the B–B  $\pi$  system is unoccupied in  $\text{YB}_6$  and  $E_F$  is instead made up of  $\sigma$  bonds. The directionality of this bonding makes it couple to the lattice much more strongly than the  $\pi$  system and an accessible crossing of states is even accessible by the phonons, an indicator of strong EPC which is not present at all in  $\text{LaB}_6$ . Softened, acoustic phonons also play a role in the  $\text{YB}_6$  EPC due to coupling to Y–Y  $\sigma$  bonds, which have no such effect in  $\text{LaB}_6$ . Finally, we show the effects of isotropic pressure and stretching on the electronic structure of these materials as it corresponds to their superconducting nature. This bonding and molecular orbital–based assessment of superconductivity paves a path for future characterization, design, and prediction of potential superconductors which is logical and accessible to any chemist.

## Materials and Methods

**Computational Methods.** DFT calculations were performed using the Vienna Ab-initio Software Package (VASP) (68, 69). Due to its excellent agreement with positron annihilation spectroscopy experiment in terms of the Fermi surface (40), the versatile PW91 exchange-correlation functional (70, 71), of the generalized gradient approximation (GGA) family of functionals, was used without any Hubbard U correction on d or f orbitals. Additionally, the calculated band structure of  $\text{LaB}_6$  is in excellent agreement with the electronic band measured by angle-resolved photoelectron spectroscopy (ARPES) (37). Furthermore, study of  $\text{YB}_6$  via photoelectron spectroscopy shows agreement with our computed DOS and the bonding picture we describe at the Fermi level (72).

Use of a van-der-Waals correction via the PBE-D3 formalism (D3 damping parameters for PW91 are not yet available) was found to have no effect on band structures or energy differences, additionally showing expected matching between the PW91 and PBE GGA functionals. Despite the fact that  $\text{LaB}_6$  and  $\text{YB}_6$  are metals and expected to be highly delocalized, the possible localization of 4f electrons in  $\text{LaB}_6$  was assessed through use of a 5 eV Hubbard U correction (73) on these orbitals applied in the rotationally invariant scheme of Dudarev et al. (74). This correction was found to change band shape (SI Appendix, Fig. S5) but

not the atomic orbital character of the frontier orbitals of  $\text{LaB}_6$  or its phonon dispersion. Unit cells, in good agreement with experimental lattice constants, were obtained from the Materials Project database (75) and their atoms' geometries were optimized in VASP to minimize forces (details below).

All DFT calculations were initially performed with the inclusion of self-consistent spin-orbit coupling (SOC) within the PAW sphere, but this was found to have no effect on the properties of interest in this study: Kohn-Sham orbital shape (assessed via real space projection of large and small spinor components), unit cell geometry and dimension, density of states (DOS), and band topology (including with the frozen phonon and its induced crossing of states in  $\text{YB}_6$ ). Specifically for DOS and band topology, no bands were inverted due to the addition of SOC, nor were relevant band degeneracies broken (SI Appendix, Fig. S6). Scalar relativistic effects remain included within the projector-augmented wave (PAW) (76) pseudopotentials of VASP. All DFT calculations were spin-unrestricted, but with the exception of extreme bond stretching at which static correlation increases and DFT begins to break down, spin-up and spin-down components were always identical. A plane-wave kinetic energy cutoff of 600 eV was used, and PAW charge densities were mixed up to angular momentum quantum number 6. Electronic energy self-consistency was enforced up to  $10^{-6}$  eV, and all-force-norm self-consistency in geometry optimization was enforced up to  $10^{-5}$  eV/Å.

Unfortunately, any changes in band structure due to post-DFT electron correlation (band renormalization) proved too computationally expensive to compute within the  $G_0W_0$  approximation, which does not require choice of Hubbard parameters as in DFT+U. Electron correlation has been shown to be crucial to properties of localized, nonconducting metal hexaborides deeper in the 4f block (6, 9), but can be considered negligible for the itinerant electronic structure of  $\text{YB}_6$  and  $\text{LaB}_6$ . This is also consistent with our benchmarking showing no need for a van-der-Waals correction and the minimal effects of localizing 4f orbitals with a Hubbard correction.

With the exception of density functional perturbation theory (DFPT) calculations requiring a 3x3x3 supercell for phonon spectra, VASP calculations were all performed using a mesh of  $21 \times 21 \times 21$  k-points using the Monkhorst-Pack scheme. This number of k-points was required for geometry optimization to ensure no presence of imaginary phonons. For DFPT calculations, the supercell size permitted 1/3 the k-points in each direction, i.e.,  $7 \times 7 \times 7$ . Fermi smearing of small width, 0.05 eV, was used in all calculations, with energies taken in the limit of zero smearing. Band structure calculations were performed with additional grid support (ADDGRID=T), and densities of states (DOS) were evaluated on 4,000 grid points. Pressure was applied to unit cells via the PSTRESS tag in VASP (minding units), and unit cells were stretched with scaled atomic distances using the Atomic Simulation Environment (77, 78).

Band and k-point resolved electron–phonon coupling magnitudes, directly proportional to phonon linewidths (taken at the fourth smearing number), were computed using Quantum Espresso (79, 80) via the same DFT parameters as in VASP and overlaid onto phonon dispersion plots. A tutorial for this procedure can be found here: <https://gitlab.com/QEF/q-e/-/tree/develop/PHonon/examples/example03>. Phonon modes were determined using the Phonopy software (81, 82) and visualized using phononwebsite (<https://henriquemiranda.github.io/phononwebsite/phonon.html>). Kohn-Sham molecular orbitals and spinors (in the case of SOC benchmarking) were plotted using the WAVECARplot (83, 84) and WaveTransPlot (85) scripts and visualized using VESTA (86–88). Phonon modes were added to VESTA-visualized unit cell files using the VaspVib2XSF script (<https://github.com/QijingZheng/VaspVib2XSF>). Electronic and phonon bands, including projected densities of states (PDOS), were plotted using the SUMO code (89).

**Data, Materials, and Software Availability.** Vibrational mode visualization files for the phonon bands of  $\text{YB}_6$  and  $\text{LaB}_6$  data can be visualized after changing extension from .txt to .yaml at phononwebsite (<https://henriquemiranda.github.io/phononwebsite/phonon.html>) (90). All other data are included in the manuscript and/or supporting information.

**ACKNOWLEDGMENTS.** R.H.L. performed the calculations on Department of Energy (DOE) National Energy Research Scientific Computing Center supercomputers under contract no. DE-AC02-05CH11231 and acknowledges support by the NSF Graduate Research Fellowship under Grant No. DGE-2034835.

An additional award of computer time was provided by the Innovative and Novel Computational Impact on Theory and Experiment program. This research used resources of the Argonne Leadership Computing Facility, which is a DOE Office of Science User Facility supported under contract DE-AC02-06CH11357. J.M. acknowledges the Spanish "Ministerio de Ciencia e Innovación" (grant number PID2021-122763NB-I00). C.E.D. acknowledges support by the NSF Graduate Research Fellowship under Grant No. DGE-2034835. F.M. acknowledges Fondo

Nacional de Desarrollo Científico y Tecnológico projects 1231487, 1220715 and by the Center for the Development of Nanosciences and Nanotechnology, CEDENNA AFB 220001. F.M. is supported by Conicyt PIA/Anillo ACT192023. Powered@The National Laboratory for High Performance Computing. This research was partially supported by the supercomputing infrastructure of the NLHPC (ECM-02). A.N.A. acknowledges Brown Science Foundation Award 1168. R.H.L. thanks Ashley Parkhurst for artistic feedback on figures.

1. R. W. Johnson, A. H. Daane, Electron requirements of bonds in metal borides. *J. Chem. Phys.* **38**, 425–432 (1963).
2. L. Zhu, G. M. Borstad, R. E. Cohen, T. A. Strobel, Pressure-induced polymorphism in  $\text{SrB}_6$  and deformation mechanisms of covalent networks. *Phys. Rev. B* **100**, 214102 (2019).
3. H. C. Longuet Higgins, M. D. V. Roberts, The electronic structure of the borides  $\text{MB}_6$ . *Proc. R. Soc. Lond. A Math. Phys. Sci.* **224**, 1158 (1954).
4. J. Kuneš, W. E. Pickett, Kondo and anti-Kondo coupling to local moments in  $\text{EuB}_6$ . *Phys. Rev. B* **69**, 165111 (2004).
5. G. Li *et al.*, Two-dimensional Fermi surfaces in Kondo insulator  $\text{SmB}_6$ . *Science* **346**, 1208–1212 (2014).
6. P. J. Robinson *et al.*, Dynamical bonding driving mixed valency in a metal boride. *Angew. Chem. Int. Ed.* **59**, 10996–110022 (2020).
7. G. E. Grecnay, A. V. Logosha, A. S. Panfilov, N. Y. Shitsevalova, Pressure effects on magnetic properties and electronic structure of  $\text{EuB}_6$  and  $\text{GdB}_6$ . *J. Alloys Compd.* **511**, 5–8 (2012).
8. I. Popov, N. Baadji, S. Sanvito, Magnetism and antiferroelectricity in  $\text{MgB}_6$ . *Phys. Rev. Lett.* **108**, 107205 (2012).
9. J. Munariz, P. J. Robinson, A. N. Alexandrova, Towards a single chemical model for understanding lanthanide hexaborides. *Angew. Chem. Int. Ed.* **59**, 22684–22689 (2020).
10. L. Sun, Q. Wu, Pressure-induced exotic states in rare earth hexaborides. *Rep. Progr. Phys.* **79**, 084503 (2016).
11. J. T. Cahill, O. A. Graeve, Hexaborides: A review of structure, synthesis and processing. *J. Mater. Res. Technol.* **8**, 6321–6335 (2019).
12. L. Xiao *et al.*, Study on the electronic structure and the optical performance of  $\text{YB}_6$  by the first-principles calculations. *AIP Adv.* **1**, 022140 (2011).
13. H. Kasai, E. Nishibori, Spatial distribution of electrons near the Fermi level in the metallic  $\text{LaB}_6$  through accurate X-ray charge density study. *Sci. Rep.* **7**, 41375 (2017).
14. Y. Zhou, F. Dai, H. Xiang, B. Liu, Z. Feng, Shear anisotropy: Tuning high temperature metal hexaborides from soft to extremely hard. *J. Mater. Sci. Technol.* **33**, 1371–1377 (2017).
15. Y. C. Zhou, B. Liu, H. M. Xiang, Z. H. Feng, Z. P. Li,  $\text{YB}_6$ : A 'ductile' and soft ceramic with strong heterogeneous chemical bonding for ultrahigh-temperature applications. *Mater. Res. Lett.* **3**, 210–215 (2015).
16. G. Schell, H. Winter, H. Rietschel, F. Gompf, Electronic structure and superconductivity in metal hexaborides. *Phys. Rev. B* **25**, 1589 (1982).
17. Z. Fisk, P. H. Schmidt, L. D. Longinotti, Growth of  $\text{YB}_6$  single crystals. *Mater. Res. Bull.* **11**, 1019–1022 (1976).
18. P. Szabó *et al.*, Superconducting energy gap of  $\text{YB}_6$  studied by point-contact spectroscopy. *Physica C* **460–462**, 626–627 (2007).
19. B. T. Matthias *et al.*, Superconductivity and antiferromagnetism in boron-rich lattices. *Science* **159**, 530 (1968).
20. O. M. Vyaselev *et al.*, Electron spin dynamics in a hexaboride superconductor  $\text{YB}_6$  probed by 89Y and 11B NMR. *J. Alloys Compd.* **921**, 165627 (2022).
21. Z. Fisk, Superconducting borides. *AIP Conf. Proc.* **231**, 155–164 (1991). <https://doi.org/10.1063/1.40864>.
22. R. Lortz *et al.*, Superconductivity mediated by a soft phonon mode: Specific heat, resistivity, thermal expansion, and magnetization of  $\text{YB}_6$ . *Phys. Rev. B* **73**, 024512 (2006).
23. V. Moshchalkov *et al.*, Type-1.5 superconductivity. *Phys. Rev. Lett.* **102**, 117001 (2009).
24. D. C. Larbalestier *et al.*, Strongly linked current flow in polycrystalline forms of the superconductor  $\text{MgB}_2$ . *Nature* **410**, 186–189 (2001).
25. J. Nagamatsu, N. Nakagawa, T. Muranaka, Y. Zenitani, J. Akimitsu, Superconductivity at 39 K in magnesium diboride. *Nature* **410**, 63–64 (2001).
26. H. Zhai, F. Munoz, A. N. Alexandrova, Strain to alter the covalency and superconductivity in transition metal diborides. *J. Mater. Chem. C. Mater.* **7**, 10700–10707 (2019).
27. S. Singh *et al.*, High-temperature phonon-mediated superconductivity in monolayer  $\text{Mg}_2\text{B}_4\text{C}_2$ . *npj Quant. Mater.* **7**, 37 (2022).
28. T. T. Pham, D. L. Nguyen, First-principles prediction of superconductivity in  $\text{MgB}_3\text{C}_3$ . *Phys. Rev. B* **107**, 134502 (2023).
29. A. B. Migdal, Interaction between electrons and lattice vibrations in a normal metal. *JETP* **34**, 996–1001 (1958).
30. G. M. Eliashberg, Interactions between electrons and lattice vibrations in a superconductor. *Sov. Phys. JETP-USSR* **11**, 696–702 (1960).
31. W. L. McMillan, Transition temperature of strong-coupled superconductors. *Phys. Rev.* **167**, 331–344 (1968).
32. P. B. Allen, R. C. Dynes, Transition temperature of strong-coupled superconductors reanalyzed. *Phys. Rev. B* **12**, 905 (1975).
33. M. I. Tsindlekht *et al.*, Linear and nonlinear low-frequency electrodynamics of surface superconducting states in an yttrium hexaboride single crystal. *Phys. Rev. B* **78**, 024522 (2008).
34. P. Szabo, P. Samuely, J. Girovsky, T. Mori, Strong coupling features in the point-contact spectra of the  $\text{YB}_6$  superconductor. *J. Phys. Conf. Ser.* **150**, 052253 (2009).
35. Y. S. Ponosov, A. A. Makhnev, S. V. Streltsov, V. B. Filippov, N. Y. Shitsevalova, Electronic Raman scattering and the electron-phonon interaction in  $\text{YB}_6$ . *JETP Lett.* **102**, 503–507 (2015).
36. M. Romero *et al.*, Ab initio calculations of the elastic, vibrational, electronic properties, and electron-phonon constant of superconducting  $\text{YB}_6$  compound under low pressure. *Phys. Scr.* **96**, 125850 (2021).
37. A. Rattanachata *et al.*, Bulk electronic structure of lanthanum hexaboride ( $\text{LaB}_6$ ) by hard X-ray angle-resolved photoelectron spectroscopy. *Phys. Rev. Mater.* **5**, 055002 (2021).
38. J. A. Alarcó, P. C. Talbot, I. D. R. Mackinnon, Comparison of functionals for metal hexaboride band structure calculations. *Model. Numer. Simul. Mater. Sci.* **04**, 53–69 (2014).
39. P. Teredesai *et al.*, High pressure phase transition in metallic  $\text{LaB}_6$ : Raman and X-ray diffraction studies. *Solid State Commun.* **129**, 791–796 (2004).
40. J. Ketels *et al.*, Fermi surface modeling of light-rare-earth hexaborides using positron annihilation spectroscopy. *Phys. Status Solidi B, Basic Res.* **259**, 2100151 (2022).
41. J. Wang *et al.*, High-pressure evolution of unexpected chemical bonding and promising superconducting properties of  $\text{YB}_6$ . *J. Phys. Chem. C* **122**, 27820–27828 (2018).
42. R. Khasanov *et al.*, Effect of pressure on the Ginzburg-Landau parameter  $\kappa = \lambda/\xi$  in  $\text{YB}_6$ . *Phys. Rev. Lett.* **97**, 157002 (2006).
43. S. Gabáni *et al.*, High-pressure effect on the superconductivity of  $\text{YB}_6$ . *Phys. Rev. B* **90**, 045136 (2014).
44. J. A. Alarcó, M. Shahbazi, P. C. Talbot, I. D. R. Mackinnon, Spectroscopy of metal hexaborides: Phonon dispersion models. *J. Raman Spectrosc.* **49**, 1985–1998 (2018).
45. Y. Xu *et al.*, First-principles study of the lattice dynamics, thermodynamic properties and electron-phonon coupling of  $\text{YB}_6$ . *Phys. Rev. B* **76**, 214103 (2007).
46. N. Sluchanko *et al.*, Lattice instability and enhancement of superconductivity in  $\text{YB}_6$ . *Phys. Rev. B* **96**, 144501 (2017).
47. P. Szabó *et al.*, Point-contact spectroscopy of the phononic mechanism of superconductivity in  $\text{YB}_6$ . *Supercond. Sci. Technol.* **26**, 045019 (2013).
48. Y. S. Ponosov, N. Y. Shitsevalova, Phonons in  $\text{YB}_6$  and  $\text{LaB}_6$ : Effects of temperature and pressure. *JETP Lett.* **102**, 295–300 (2015).
49. H. J. Choi, D. Roundy, H. Sun, M. L. Cohen, S. G. Louie, The origin of the anomalous superconducting properties of  $\text{MgB}_2$ . *Nature* **418**, 758–760 (2002).
50. H. W. T. Morgan, A. N. Alexandrova, Electron counting and high-pressure phase transformations in metal hexaborides. *Inorg. Chem.* **61**, 18701–18709 (2022).
51. J. Bardeen, L. N. Cooper, J. R. Schrieffer, Theory of superconductivity. *Phys. Rev.* **108**, 1175 (1957).
52. P. J. Robinson, X. Zhang, T. McQueen, K. H. Bowen, A. N. Alexandrova,  $\text{SmB}_6$ -cluster anion: Covacency involving f orbitals. *J. Phys. Chem. A* **121**, 1849–1854 (2017).
53. H. Liu, I. I. Naumov, R. Hoffmann, N. W. Ashcroft, R. J. Hemley, Potential high-Tc superconducting lanthanum and yttrium hydrides at high pressure. *Proc. Natl. Acad. Sci. U.S.A.* **114**, 6960–6995 (2017).
54. S. Adhikari, P. Mukhopadhyay, Physical metallurgy of beryllium and its alloys. *Miner. Process. Extr. Metall. Rev.* **14**, 253–299 (1995).
55. S. Maintz, V. L. Deringer, A. L. Tchougréff, R. Dronskowski, LOBSTER: A tool to extract chemical bonding from plane-wave based DFT. *J. Comput. Chem.* **37**, 1030–1035 (2016).
56. R. Peierls, *More surprises in theoretical physics* (Princeton University Press, Princeton, NJ, 1991). <https://doi.org/10.2307/j.ctv10crq2s>.
57. P. W. Anderson, P. A. Lee, M. Saitoh, Remarks on giant conductivity in TTF-TCNO. *Solid State Commun.* **13**, 595–598 (1973).
58. R. E. Thorne, Charge-density-wave conductors. *Phys. Today* **49**, 42–47 (1996).
59. K. P. Hilleke, T. Bi, E. Zurek, Materials under high pressure: A chemical perspective. *Appl. Phys. A, Mater. Sci. Process.* **128**, 441 (2022).
60. P. J. Robinson, A. N. Alexandrova, Assessing the bonding properties of individual molecular orbitals. *J. Phys. Chem. A* **119**, 12862–12867 (2015).
61. J. Lei *et al.*, Understanding how bonding controls strength anisotropy in hard materials by comparing the high-pressure behavior of orthorhombic and tetragonal tungsten monoboride. *J. Phys. Chem. C* **122**, 5647–5656 (2018).
62. Y. Zhou *et al.*, Pressure-induced quantum phase transitions in a  $\text{YbB}_6$  single crystal. *Phys. Rev. B* **92**, 241118 (2015).
63. G. Weill, I. A. Smirnov, V. N. Gurin, Electrical transport properties of  $\text{EuB}_6$  under pressure. New experimental data. *Phys. Status Solidi A* **53**, 119–123 (1979).
64. T. Sakai, G. Oomi, Y. Uwamoto, S. Kunii, Effect of pressure on the metamagnetic transition of  $\text{DyB}_6$  single crystal. *J. Magn. Magn. Mater.* **310**, 1732–1734 (2007).
65. N. P. Butch *et al.*, Pressure-resistant intermediate valence in the kondo insulator  $\text{SmB}_6$ . *Phys. Rev. Lett.* **116**, 156401 (2016).
66. A. Stern, M. Dzero, V. M. Galitski, Z. Fisk, J. Xia, Surface-dominated conduction up to 240 K in the Kondo insulator  $\text{SmB}_6$  under strain. *Nat. Mater.* **16**, 708–711 (2017).
67. C. H. Chen, T. Aizawa, N. Iyi, A. Sato, S. Otani, Structural refinement and thermal expansion of hexaborides. *J. Alloys Compd.* **366**, 6–8 (2004).
68. G. Kresse, J. Hafner, Ab initio molecular dynamics for liquid metals. *Phys. Rev. B* **47**, 558 (1993).
69. G. Kresse, J. Furthmüller, Efficient iterative schemes for ab initio total-energy calculations using a plane-wave basis set. *Phys. Rev. B* **54**, 11169 (1996).
70. J. P. Perdew, Y. Wang, Accurate and simple analytic representation of the electron-gas correlation energy. *Phys. Rev. B* **45**, 13244 (1992).
71. J. P. Perdew *et al.*, Atoms, molecules, solids, and surfaces: Applications of the generalized gradient approximation for exchange and correlation. *Phys. Rev. B* **46**, 6671 (1992).
72. S. Souma *et al.*, Direct observation of superconducting gap in  $\text{YB}_6$  by ultrahigh-resolution photoemission spectroscopy. *J. Electron. Spectrosc. Relat. Phenom.* **144–147**, 503–506 (2005).
73. W. L. Li, C. Ertural, D. Bogdanovski, J. Li, R. Dronskowski, Chemical bonding of crystalline  $\text{LnB}_6$  ( $\text{Ln} = \text{La-Lu}$ ) and its relationship with  $\text{Ln}_2\text{B}_6$  gas-phase complexes. *Inorg. Chem.* **57**, 12999–13008 (2018).
74. S. Dudarev, G. Botton, Electron-energy-loss spectra and the structural stability of nickel oxide: An LSDA+U study. *Phys. Rev. B* **57**, 1505 (1998).
75. A. Jain *et al.*, Commentary: The materials project: A materials genome approach to accelerating materials innovation. *APL Mater.* **1**, 011002 (2013).
76. P. E. Blöchl, Projector augmented-wave method. *Phys. Rev. B* **50**, 17953 (1994).

77. A. Hjorth Larsen *et al.*, The atomic simulation environment—A Python library for working with atoms. *J. Phys. Condens. Matter* **29**, 273002 (2017).
78. S. R. Bahn, K. W. Jacobsen, An object-oriented scripting interface to a legacy electronic structure code. *Comput. Sci. Eng.* **4**, 56–66 (2002).
79. P. Giannozzi *et al.*, QUANTUM ESPRESSO: A modular and open-source software project for quantum simulations of materials. *J. Phys. Condens. Matter* **21**, 395502 (2009).
80. P. Giannozzi *et al.*, Advanced capabilities for materials modelling with Quantum ESPRESSO. *J. Phys. Condens. Matter* **29**, 465901 (2017).
81. A. Togo, First-principles phonon calculations with phonopy and phono3py. *J. Phys. Soc. Japan* **92**, 012001 (2023).
82. A. Togo, I. Tanaka, First principles phonon calculations in materials science. *Scr. Mater.* **108**, 1–5 (2015).
83. K. Czelej, M. R. Zemla, P. Kamińska, P. Śpiewak, K. J. Kurzydłowski, Clustering of hydrogen, phosphorus, and vacancies in diamond: A density functional theory analysis. *Phys. Rev. B* **98**, 075208 (2018).
84. K. Czelej, K. Ćwieka, P. Śpiewak, K. J. Kurzydłowski, Titanium-related color centers in diamond: A density functional theory prediction. *J. Mater. Chem. C* **6**, 5261–5268 (2018).
85. R. M. Feenstra *et al.*, Low-energy electron reflectivity from graphene. *Phys. Rev. B* **87** (2013).
86. K. Momma, F. Izumi, VESTA: A three-dimensional visualization system for electronic and structural analysis. *J. Appl. Crystallogr.* **41**, 041406 (2008).
87. K. Momma, F. Izumi, An integrated three-dimensional visualization system VESTA using wxWidgets. *Comm. Crystallogr. Comput. IUCr Newslett.* **7**, 106–119 (2006).
88. K. Momma, F. Izumi, VESTA 3 for three-dimensional visualization of crystal, volumetric and morphology data. *J. Appl. Crystallogr.* **44**, 1272–1276 (2011).
89. A. M. Ganose, A. J. Jackson, D. O. Scanlon, sumo: Command-line tools for plotting and analysis of periodic ab initio calculations. *J. Open Source Software* **3**, 717 (2018).
90. E. Miranda, Phonon website. <https://henriquemiranda.github.io/phononwebsite/phonon.html>. Accessed 14 March 2023.